# Semi-Lagrangian Advection on Conformal-Cubic Grids

JOHN L. MCGREGOR

*CSIRO Division of Atmospheric Research, Melbourne, Victoria, Australia*

(Manuscript received 18 July 1995, in final form 12 December 1995)

ABSTRACT

It has been demonstrated by McGregor that semi-Lagrangian advection techniques may be efficiently applied to a cubic gnomonic grid on the sphere. Despite the nonorthogonal nature of that grid, the accuracy is superior to that of conventional latitude–longitude grids. The present paper demonstrates even greater accuracy by applying similar techniques to the related conformal-cubic grid devised by Rančić et al.; an important new feature is a simple iterative technique for the inverse calculation of grid coordinates. Advection over the vertices of the grid exhibits none of the problems that occur over the poles of a latitude–longitude grid. A stretched grid configuration is also presented showing further improvements. It is finally shown that the departure points may be interpolated onto a B-grid version and advection performed simply on the staggered grid without loss of accuracy.

## 1. Introduction

Most global meteorological models are based on a regular latitude–longitude configuration either explicitly, or implicitly, in the case of a spectral formulation. There are, however, advantages in being able to use a grid having more uniform resolution, for reasons of computational economy for a given accuracy and for uniform applicability of physical parameterizations. With this in mind, Sadourny (1972) proposed a grid derived from a gnomonic projection of the cube onto the sphere and presented corresponding solutions of the shallow-water equations. The projection produces six panels covering the sphere; Sadourny (1972) experienced noise problems that he attributed to his low-order finite differencing near the panel edges. McGregor (1996, denoted here by M96) adopted the same grid and demonstrated that the semi-Lagrangian technique of McGregor (1993) permits accurate and noise-free solutions for horizontal advection. With this grid, although the projected grid lines on the cube are orthogonal, the grid lines on the sphere are nonorthogonal. M96 also investigated stretched grids having the same nonorthogonality properties but producing greater uniformity on the sphere and even better advection results.

The nonorthogonality of the M96 grid creates only slight inconvenience for advection purposes, but the full primitive equations are significantly simpler on an orthogonal grid. Fortunately Rančić et al. (1996, denoted hereafter by RPM) have found a solution to this problem. RPM employ the same Sadourny (1972) projection from the panels of a cube onto the sphere. By means of a conformal mapping with respect to a stereographic projection, they have devised a set of grid lines on each panel of the sphere that are orthogonal to one another except at the vertices where they intersect at 120°. The grid may be described as a "conformal-cubic" grid and is an example of a modified cubic gnomonic projection. The RPM paper is concerned with geometrical properties of the grid; it also successfully provides Eulerian finite-difference solutions to the shallow-water equations.

Sadourny (1972), M96, and the present paper produce grids on projections of panels of a cube encompassing the sphere. RPM equivalently use a projection from a cube contained within the sphere, referring to the grid as an "expanded cube." Figure 1a shows a view from infinity of the RPM conformal-cubic grid possessing 8216 grid points, which is similar in number to the 8192 grid points of an R42 Gaussian grid. This grid is used for the advection tests in this paper, oriented as in M96 such that the North Pole and 0°, 0° are each in the center of panels.

The grid of RPM possesses higher resolution near the vertices. For a semi-Lagrangian primitive equations model, it may be preferable not to have the finest resolution over steep orography. This is because stationary resonances may occur over steep orography if the Courant number exceeds unity (e.g., Rivest et al. 1994). To illustrate that it should be possible to avoid such resonances in a full model without greatly restricting the time step, Fig. 2 shows that the conformal-cubic grid can be oriented on the earth such that each vertex

*Corresponding author address:* Dr. John L. McGregor, CSIRO, Division of Atmospheric Research, Private Bag No. 1 Aspendale, Victoria 3195, Australia.
E-mail: jlm@dar.csiro.au

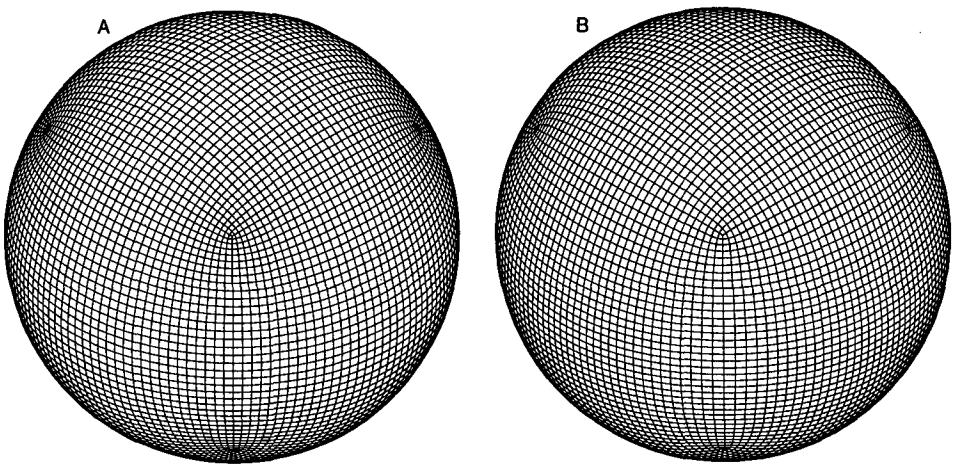


FIG. 1. A view from infinity of the RPM cubic grids, (a) the standard RPM conformal-cubic grid, and (b) the stretched $\alpha = 0.875$ grid, both for $N = 37$.

is located over the sea apart from a single vertex over the West Siberian plain.

The present paper employs the algorithms of RPM to determine the grid locations, map factors, and the unit vectors along the axes. The semi-Lagrangian method of McGregor (1993) is then applied to the same set of test cases as in M96, as well as to a case where a cosine bell is advected directly over the vertices. Comparisons for stretched versions of the grid are also presented.

## 2. Grid transformations

### a. Grid indexing and gnomonic transformations

The notation of M96 is kept for the coordinate representations on the sphere and for the gnomonic projections onto a cube that is created encompassing the sphere and tangent to it. Cartesian 3D coordinates are given as upper case: $(X, Y, Z)$ on the sphere and $(A, B, C)$ on the projected cube. Local 2D coordinates on the surface of a panel $p$ are written in lower case: $(x, y, p)$ on the sphere and $(a, b, p)$ on the projected cube, where $0 \leq p \leq 5$. In M96 the $(x, y)$ coordinates on the sphere were not orthogonal, although the $(a, b)$ coordinates on the cube were orthogonal. In the present paper, the RPM transformation produces orthogonal $(x, y)$ coordinates on the sphere apart from the vertices themselves; the projected $(a, b)$ coordinates on the cube are not orthogonal.

The orientation of the panels and of the $x$ and $y$ axes is given in Fig. 1 of M96; that paper also describes the relationship between the overlapping indexing of neighboring panels. Each panel edge has $N$ segments and each panel contains $N \times N$ quadrilateral elements. On each panel the range of $x$ and $y$ is $-R \leq x \leq R$, $-R \leq y \leq R$, where $R$ is the radius of the sphere. The grid increments are $\Delta x = \Delta y = 2R/N$, and corresponding physical displacements are $\Delta x/m$ and $\Delta y/m$; $m$ is a map factor (equal to $4/\pi$ on average along a great circle passing through four panel centers). M96 provides the transformations between the $(X, Y, Z)$, $(A, B, p)$, and $(a, b, p)$ representations; for convenience these are summarized in appendix A.

### b. Grid information supplied by the RPM routines

The RPM routines are used to produce $(X, Y, Z)$, map factors and unit tangential vectors at grid points on panel 0 of the sphere. The corresponding $(a, b)$ on panel 0 of the cube are then calculated. Values for $(a, b)$ on the other panels follow easily from symmetry; these $(a, b)$ are then projected back to give the remaining $(X, Y, Z)$ on the sphere. Tangential vectors on the other panels are calculated using the relationships given in appendix B.

Nonintegral grid values are needed only for determining staggered B-grid locations (obtainable from a double resolution grid) and for the quadruple resolution grid used in the inverse calculations of appendix C. The double and quadruple resolution grids (needed only for one panel) are provided by the RPM algorithms using two and four times as many points, respectively, in each direction. Note that the coarser grid points align exactly with grid points of the higher-resolution grids.

### c. Map factors and stretched grids

It is required to calculate space increments $D_x$ and $D_y$ along the $x$ and $y$ coordinate axes on the panels of the sphere. The RPM routines provide a map factor $m$, such that

$$D_x = \frac{\Delta x_R}{m}, \tag{1}$$

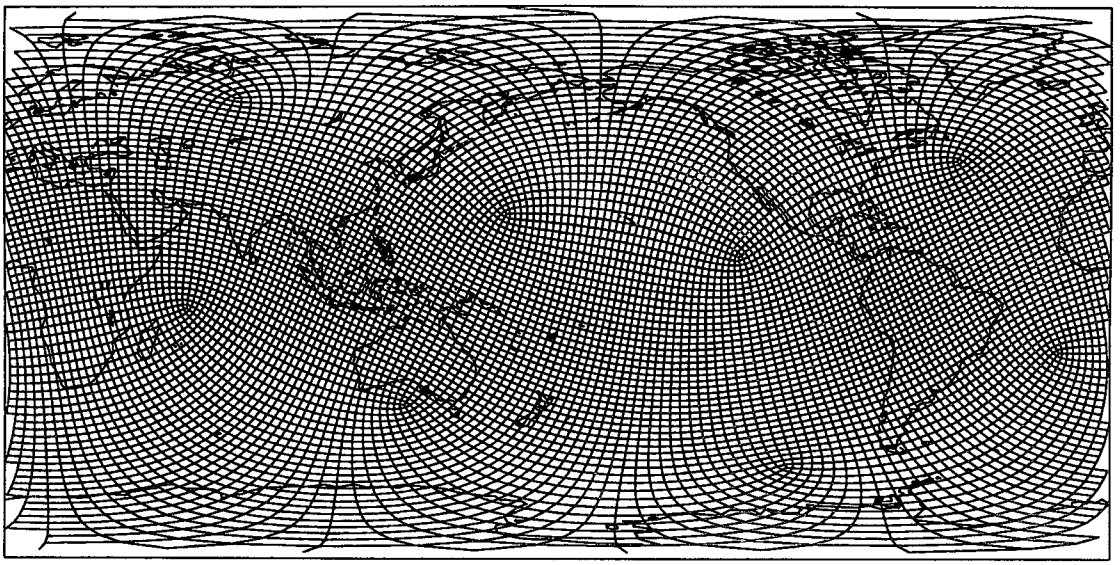

FIG. 2. Suggested grid configuration in which all vertices are located over flat areas, displayed on a latitude–longitude projection. This grid orientation would have advantages for a primitive equations model.

where $-R \leq x_R \leq R$ and $\Delta x_R$ is an increment in $x_R$, the (unstretched) RPM $x$ map coordinate. Similarly to M96, in order to further improve the uniformity of resolution, a cubic stretching can be provided,

$$x_R = \alpha x + (1 - \alpha)\frac{x^3}{R^2}, \qquad (2)$$

where $-R \leq x \leq R$ and $\alpha$ is a constant. This stretching does not affect $x$ values at the panel edges. Given a set of prescribed $x$ values, (2) provides a corresponding set of $x_R$ values, then used by the RPM routines to supply 3D Cartesian $(X, Y, Z)$, map factors, and unit tangential vectors. The stretching effect of $\alpha$ is different to that of $\alpha$ in M96, being applied on the sphere rather than on the projected cube. Differentiating (2), the space increment relationship becomes

$$D_x = \frac{\Delta x_R}{m} = [\alpha + 3(1 - \alpha)x^2]\frac{\Delta x}{m}, \qquad (3)$$

where the utilized grid increments are $\Delta x = 2R/N$. There is a similar expression for space increments along the $y$ axes. There are then two different effective map factors affecting $\Delta x$ and $\Delta y$,

$$m_x = \frac{m}{\alpha + 3(1 - \alpha)x^2},$$

$$m_y = \frac{m}{\alpha + 3(1 - \alpha)y^2}. \qquad (4)$$

With only slight loss in accuracy, the space increments $D_x$ and $D_y$ along the $x$ and $y$ axes may alternatively be evaluated as in M96 by finite differencing of the neighboring gridpoint Cartesian locations. This approach is used at the vertices, where the map factors are singular. Figure 1b shows a stretched RPM grid with $\alpha = 0.875$. In both the standard RPM grid ($\alpha = 1$) and the stretched version, the maximum grid length is midway along an edge and perpendicular to it ($0.0818R$ for $\alpha = 1$, $0.1023R$ for $\alpha = 0.875$), while the minimum occurs at vertices ($0.0262R$ for $\alpha = 1$, $0.0344R$ for $\alpha = 0.875$); these values are for an $N = 37$ grid. The ratio of maximum-to-minimum grid length is 3.13 (for $\alpha = 1$), dropping slightly to 2.96 (for $\alpha = 0.875$). The stretched grid is thus slightly more uniform than the unstretched grid. The corresponding ratios for the nonorthogonal M96 grid are 2.1 (for $\alpha = 1$) and 1.5 (for $\alpha = 0.75$), whereas for a T42 Gaussian grid the ratio of maximum to minimum longitudinal grid increment is 26.8.

### *d. Inverse calculation of grid coordinates from the 3D Cartesian positions*

The semi-Lagrangian procedure to be described in section 3 produces departure points on the sphere in terms of the 3D Cartesian coordinates $(X, Y, Z)$. Subsequent interpolations to obtain field values require those departure points to be expressed in terms of indices and panel numbers. This is most readily determined by calculations projected onto the faces of the cube, where the number of spatial dimensions has been reduced from three to two. Note that indices and panel numbers on the sphere are identical to those of the projected point on the cube.

The nonorthogonal grid used by M96 provides analytic expressions for the grid indices given these $(a, b)$ values on the cube. Such expressions are not

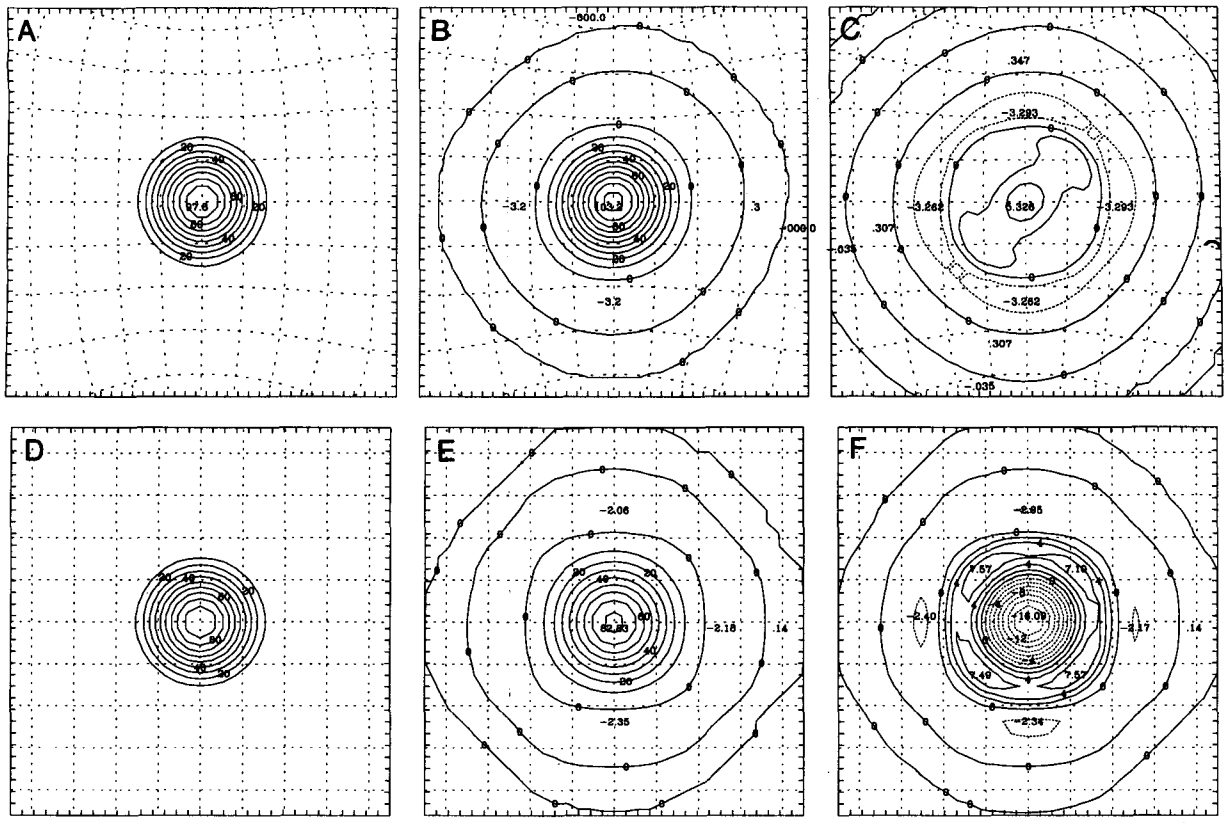


FIG. 3. Northeastward advected cosine bell with 256 time steps per solid-body rotation. On one panel of the standard RPM $N = 37$ conformal-cubic grid after one rotation are shown (a) verifying heights, (b) advected heights, and (c) errors. On the T42 Gaussian grid after one rotation are shown (d) verifying heights, (e) advected heights, and (f) errors. Latitudes and longitudes are shown every 10°. Height contours are drawn every 10 units and error contours every 2 units.

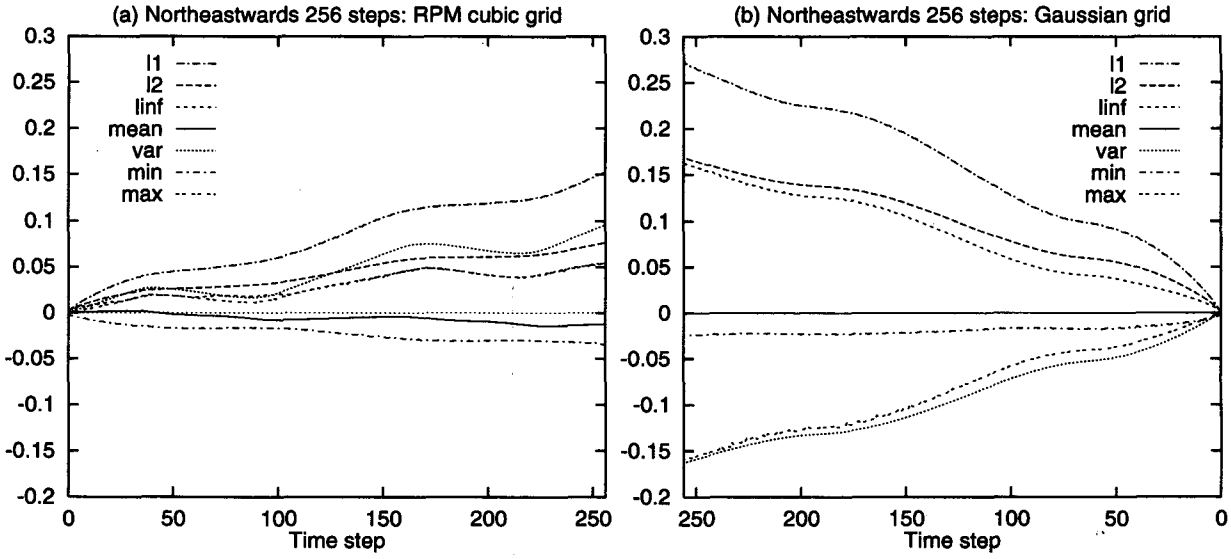


FIG. 4. Time traces of the normalized errors for the northeastward advection test of Fig. 3 with 256 time steps for (a) the standard RPM cubic grid and (b) the T42 Gaussian grid. The second plot is plotted from right to left to assist comparisons.

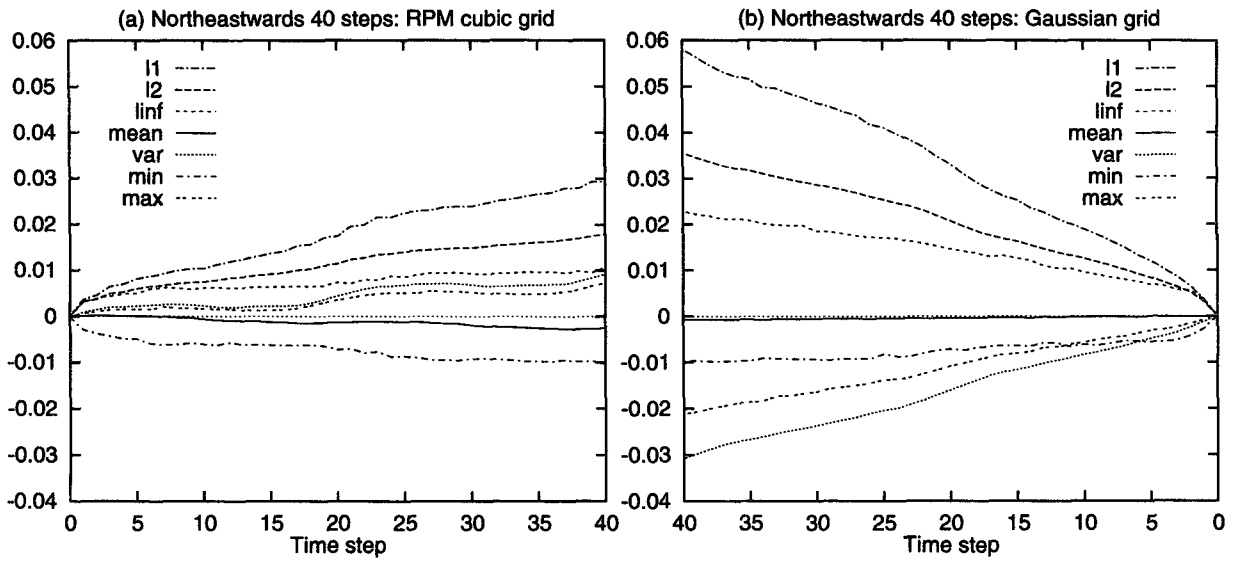


FIG. 5. Time traces of the normalized errors as in Fig. 4 but with 40 time steps per solid-body rotation.

available for the RPM grid with its more complicated $(a, b)$ spacing; it appeared initially that this could inhibit the use of semi-Lagrangian methods on this grid. However, as described in appendix C, a technique has been devised whereby the indices are determined by simple iterations (two iterations in practice) performed on the faces of the cube using a quadruple resolution grid. For this iterative cal-

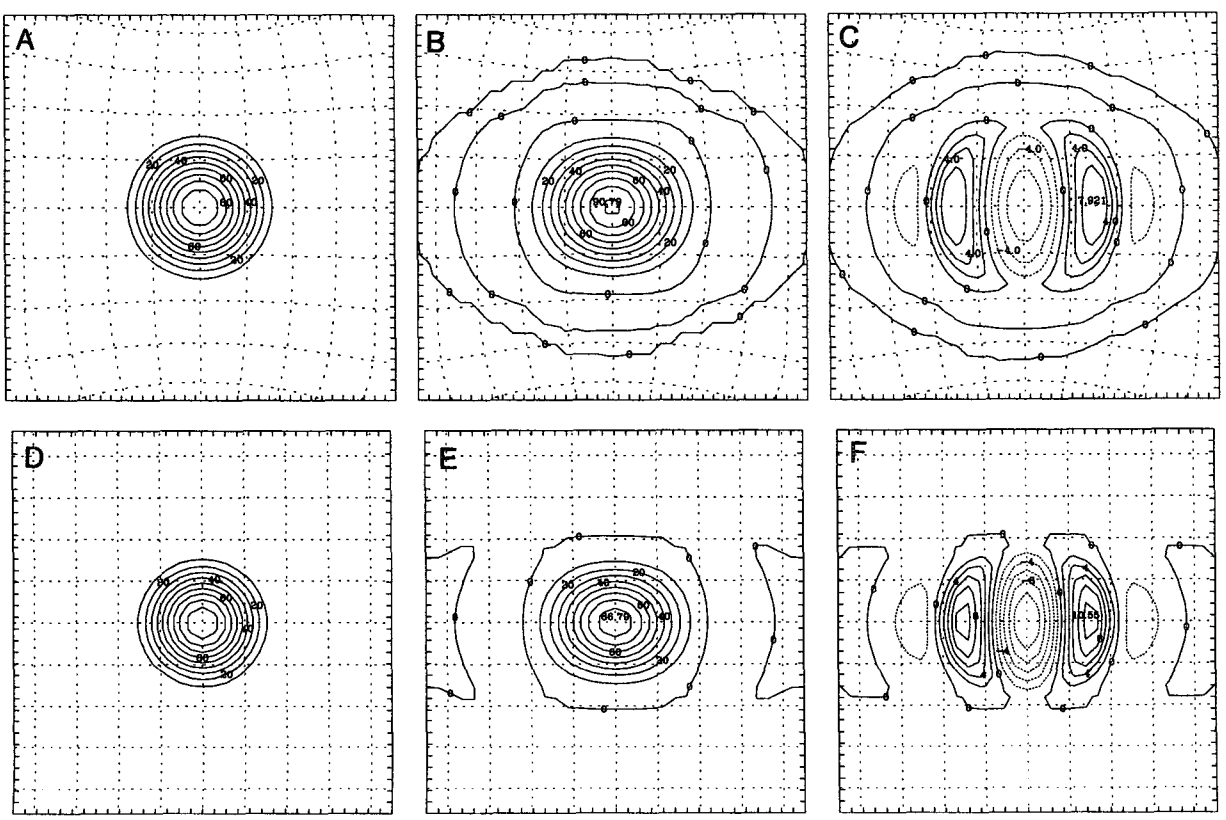


FIG. 6. As in Fig. 3 but for the eastward advected cosine bell. (a)–(c) The stretched $\alpha = 0.875$ RPM cubic grid.(d)–(f) The T42 Gaussian grid.

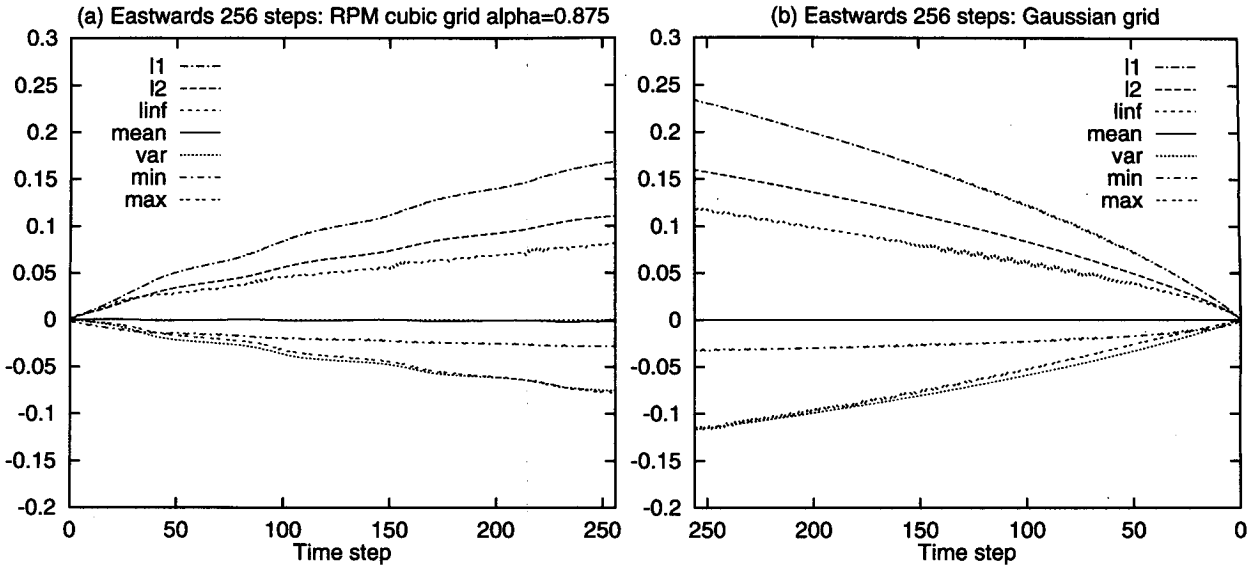


FIG. 7. Time traces of the normalized errors for the eastward advection test of Fig. 6 with 256 time steps for (a) the stretched $\alpha = 0.875$ RPM cubic grid and (b) the T42 Gaussian grid. The second plot is plotted from right to left to assist comparisons.

culation, the quadruple resolution grid performed more accurately than a double-resolution grid. An eight-times resolution grid produced no extra benefits. Note that the computation time for this inverse calculation is independent of the resolution of the iterative grid.

## 3. Advection and interpolation on the conformal-cubic grid

Horizontal advection on the sphere of a scalar field $\phi$ may be written as

$$\frac{d\phi}{dt} = 0, \tag{5}$$

where

$$\frac{d}{dt} = \frac{\partial}{\partial t} + m_x u \frac{\partial}{\partial x} + m_y v \frac{\partial}{\partial y} \tag{6}$$

and where $u \equiv m_x^{-1}(dx/dt)$ and $v \equiv m_y^{-1}(dy/dt)$ are the physical velocity components along the $x$ and $y$ coordinates. The $m_x$ and $m_y$ map factors are equal to one another for the standard ($\alpha = 1$) RPM grid. The two-

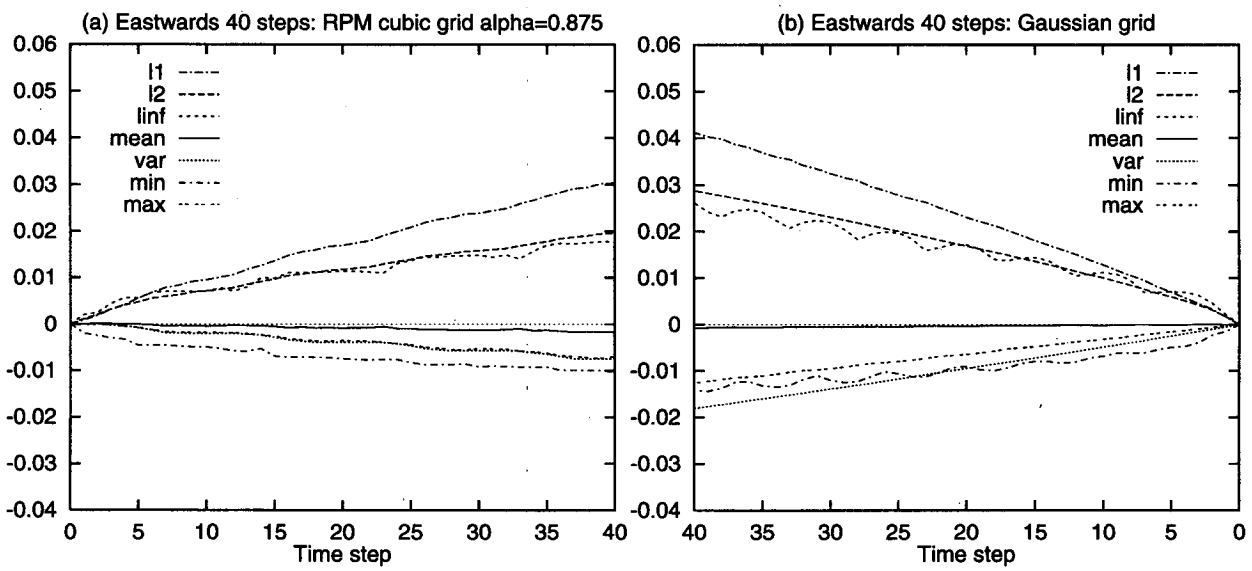


FIG. 8. Time traces of the normalized errors as in Fig. 7 but with 40 time steps per solid-body rotation.

TABLE 1. Normalized $l_1$ errors (as %) after one solid-body rotation (with 40 time steps per rotation). The Gaussian hill test was proposed by Ritchie (1987). The cosine bell tests of Williamson et al. (1992) proceed initially in N, E, $N^+$, and $E^-$ directions; an extra test advecting initially NE is included. Results are shown in three main groups: the T42 Gaussian grid and nonorthogonal grids of M96; the standard and stretched RPM cubic grids with $N = 37$; the staggered RPM B grids. The smallest error for each test is boldface. The final two columns provide a comparison between a lower-resolution RPM grid with $N = 30$ and a reduced T42 Gaussian grid.

| | Gaussian grid | M96 $\alpha = 1$ | M96 $\alpha = 0.75$ | RPM $\alpha = 1$ | RPM $\alpha = 0.875$ | RPM-B $\alpha = 1$ | RPM-B $\alpha = 0.875$ | RPM-30 $\alpha = 1$ | Reduced Gaussian |
|---|---|---|---|---|---|---|---|---|---|
| Gaussian hill | 19.6 | 17.2 | 13.2 | 14.6 | 11.8 | 14.7 | **11.5** | 23.0 | 22.7 |
| N/E | 5.0/4.1 | 4.4 | 4.2 | 3.6 | **3.0** | 3.7 | 3.1 | 3.6 | 5.7/4.0 |
| $N^+/E^-$ | 5.0/5.4 | 4.6 | 4.2 | 3.1 | **2.6** | 3.2 | 2.7 | 4.0 | 6.1/5.4 |
| NE | 5.8 | 3.9 | 3.3 | 2.9 | **2.5** | 3.0 | 2.6 | 4.1 | 6.6 |

time-level semi-Lagrangian solution at a new time step is

$$\phi(\tau + \Delta\tau) = \phi^*(\tau), \tag{7}$$

where $\phi^*(\tau)$ is the value of $\phi$ evaluated by interpolation at the upstream departure point at time $\tau$.

### a. Derivation of the departure points

Following McGregor (1993) the departure points of the 3D grid point located at $\mathbf{r}(\tau + \Delta t)$ can be written in terms of the truncated Taylor series of the total derivatives

$$\mathbf{r}(\tau) \approx \mathbf{r}(\tau + \Delta t) + \sum_{n=1}^{3} \frac{(-\Delta t)^n}{n!} \frac{d^n\mathbf{r}}{dt^n}(\tau + \Delta t), \tag{8}$$

where

$$\frac{d^n\mathbf{r}(t)}{dt^n} = \frac{d}{dt}\left[\frac{d^{n-1}\mathbf{r}(t)}{dt^{n-1}}\right] \quad n = 2, 3. \tag{9}$$

The solution is second-order accurate in time provided that $d/dt$ is evaluated using (6) without the partial time derivative term, but with velocities centered at time $\tau + \Delta t/2$. As in M96, the higher material derivatives in (8) are evaluated by application of (6) with simple centered finite differences. For the first term of the Taylor series in (8), the 3D Cartesian velocity components are used directly. This produces greater accuracy for the RPM grid than using a finite difference version of (6) to evaluate this term.

Equation (8) is applied separately to each Cartesian component in the form $(X, Y, Z)$ to give corresponding departure point values; the two-iteration inverse procedure of section 2 then gives the equivalent departure points in terms of $(i, j, p)$, where $i$ and $j$ are nonintegral grid indices. As in M96, the use of Cartesian components allows the determination of departure points to pass over panel boundaries in a transparent manner. Some extra economy in the computations may be achieved by first normalizing the velocity components $u$ and $v$ to units of grid point per time step.

As in M96, at the eight vertices the material derivative (6) is replaced by an uncentered derivative expression

$$\frac{d}{dt} = \frac{\partial}{\partial t} + \frac{2}{9} m(4u_q + u_r + u_s)\frac{\partial}{\partial x_q} + \frac{2}{9} m(u_q + 4u_r + u_s)\frac{\partial}{\partial x_r} + \frac{2}{9} m(u_q + u_r + 4u_s)\frac{\partial}{\partial x_s}, \tag{10}$$

where $u_q$, $u_r$, and $u_s$ denote the velocity components in the directions of the three intersecting axes. As stated earlier, the space increments of the form $\Delta x/m$ are evaluated by finite differences at the vertices.

### b. Interpolation of field values

During an advective calculation, the values $(i, j, p)$ are used to determine the value of the advected $\phi$ field via quasi-bicubic interpolation centered on a $4 \times 4$ stencil. Quasi-cubic interpolation was suggested by Philippe Courtier; it is used in the operational ECMWF model and is described by Ritchie et al. (1995). During the first direction of interpolation, linear interpolations

TABLE 2. As in Table 1 but for the normalized $l_2$ errors (%).

| | Gaussian grid | M96 $\alpha = 1$ | M96 $\alpha = 0.75$ | RPM $\alpha = 1$ | RPM $\alpha = 0.875$ | RPM-B $\alpha = 1$ | RPM-B $\alpha = 0.875$ | RPM-30 $\alpha = 1$ | Reduced Gaussian |
|---|---|---|---|---|---|---|---|---|---|
| Gaussian hill | 15.7 | 14.5 | 11.2 | 10.7 | **8.8** | 10.8 | **8.8** | 16.5 | 18.0 |
| N/E | 3.1/2.9 | 2.8 | 2.6 | 2.3 | **2.0** | 2.3 | **2.0** | 2.3 | 3.5/2.9 |
| $N^+/E^-$ | 3.1/3.4 | 2.9 | 2.6 | 2.1 | **1.8** | 2.1 | **1.8** | 2.5 | 3.7/3.4 |
| NE | 3.6 | 2.4 | 2.0 | 1.9 | **1.6** | 1.8 | **1.6** | 2.5 | 4.1 |

TABLE 3. As in Table 1 but for the normalized $l_\infty$ errors (%).

| | Gaussian grid | M96 $\alpha = 1$ | M96 $\alpha = 0.75$ | RPM $\alpha = 1$ | RPM $\alpha = 0.875$ | RPM-B $\alpha = 1$ | RPM-B $\alpha = 0.875$ | RPM-30 $\alpha = 1$ | Reduced Gaussian |
|---|---|---|---|---|---|---|---|---|---|
| Gaussian hill | 20.7 | 18.1 | 14.7 | 12.8 | **11.2** | 14.2 | 12.0 | 21.6 | 23.3 |
| N/E | 2.9/2.6 | 2.0 | 1.8 | 2.0 | 1.8 | 1.9 | **1.7** | 1.5 | 2.3/2.6 |
| $N^+/E^-$ | 2.2/2.4 | 2.0 | 1.7 | 1.6 | 1.4 | 1.5 | **1.3** | 1.7 | 2.2/2.4 |
| NE | 2.3 | 1.6 | 1.5 | 1.1 | **1.0** | **1.0** | 1.1 | 1.7 | 2.6 |

are performed along the edges of the 4 × 4 stencil. This reduces the stencil to effectively 12 points but maintains high accuracy. The reduced stencil also provides some simplifications near the vertices.

During even time steps, $x$–$y$ interpolation is performed ($x$ interpolation before $y$ interpolation); during odd time steps $y$–$x$ interpolation is performed. Analogously to the splitting methods of Marchuk (1974), this alternation should produce some error reduction. The advection tests are found to be quite insensitive to the starting order of the alternating interpolations; conversely, some sensitivity is found if only nonalternating interpolation is used.

Within any quadrilateral element adjacent to a vertex, there is a choice in how to extend the edge points to provide the fourth point for cubic interpolation; either of the two adjacent points on the other edges or some combination of the other points could be chosen. The advection tests in this paper were found to be very insensitive to that choice, probably because the grid resolution is finest near the vertices.

It should be mentioned that the interpolations on the nonorthogonal grids of M96 were performed wholly within panels and thus near the panel edges the interpolations were not centered on the 4 × 4 stencils. It was noted in that paper that the uncentered locations might sometimes produce weak resonant instabilities near orography in a full primitive equations model. The present scheme always uses centered stencils, avoiding such an eventuality.

### c. *Advection on a B-grid version*

For future application of the conformal-cubic grid to the shallow-water or primitive equations, it is likely that a staggered grid will be preferred. At present the B-grid appears most suitable with the velocity components located at the grid points shown in Fig. 1 and the mass variables located at the center of each quadrilateral grid element. The grid decoupling experienced with a nonstaggered grid (for example, Mesinger and Arakawa 1976; McGregor and Leslie 1977) will be greatly reduced by tight coupling of the solutions in the vicinity of each vertex. This can be seen by selecting a mass point and observing that it is linked closely to all other mass points near a vertex, through the pressure gradient and velocity divergence terms. The coupling is tightest at a vertex because evaluation of any component of the pressure gradient term at a vertex involves all three neighboring mass points. The tight coupling is lost if the mass and wind points are allocated in the reverse configuration. The locations of the staggered points are chosen to be coincident with an unstaggered grid having double the resolution.

The results of the following section demonstrate that one may use the same departure point information calculated above but interpolated with a bicubic scheme to give departure points at the staggered grid locations. This involves less computation than a separate complete determination of the departure points. A similar determination of staggered grid departure points (on a C grid) is successfully employed in the two-time-level semi-Lagrangian Division of Atmospheric Research limited-area model (DARLAM) described by McGregor et al. (1993). The 3D departure points available for the nonstaggered grid locations are interpolated with a cubic scheme to the midpoint of each grid segment (uncentered adjacent to the vertices), then to the staggered locations. There is no computational saving in using quasi-bicubic rather than full bicubic interpolation for this calculation.

The subsequent interpolation of field values on the B grid is carried out as at the unstaggered locations by alternating each time step between $x$–$y$ and $y$–$x$ quasi-cubic interpolations. Although the 12-point interpola-

TABLE 4. As in Table 1 but for the normalized error of the mean (%).

| | Gaussian grid | M96 $\alpha = 1$ | M96 $\alpha = 0.75$ | RPM $\alpha = 1$ | RPM $\alpha = 0.875$ | RPM-B $\alpha = 1$ | RPM-B $\alpha = 0.875$ | RPM-30 $\alpha = 1$ | Reduced Gaussian |
|---|---|---|---|---|---|---|---|---|---|
| Gaussian hill | 0.22 | −0.22 | **−0.14** | 0.54 | −0.23 | 0.54 | −0.23 | −0.82 | 0.29 |
| N/E | 0.25/**−0.08** | 0.55 | **0.13** | −0.25 | −0.17 | −0.25 | −0.18 | 0.03 | 0.28/−0.08 |
| $N^+/E^-$ | 0.02/−0.08 | 0.25 | **0.01** | −0.05 | −0.03 | −0.05 | −0.04 | −0.10 | 0.15/−0.08 |
| NE | −0.07 | **−0.06** | 0.10 | −0.25 | −0.40 | −0.25 | −0.35 | −0.11 | −0.07 |

TABLE 5. As in Table 1 but for the normalized error of the variance (%).

| | Gaussian grid | M96 $\alpha = 1$ | M96 $\alpha = 0.75$ | RPM $\alpha = 1$ | RPM $\alpha = 0.875$ | RPM-B $\alpha = 1$ | RPM-B $\alpha = 0.875$ | RPM-30 $\alpha = 1$ | Reduced Gaussian |
|---|---|---|---|---|---|---|---|---|---|
| Gaussian hill | −13.4 | −13.4 | −9.8 | −5.4 | −5.1 | −5.4 | **−5.0** | −12.9 | −15.6 |
| N/E | −1.66/−1.81 | −1.22 | −1.46 | −0.95 | **−0.75** | −0.96 | −0.76 | −0.76 | −2.10/−1.80 |
| $N^+/E^-$ | −2.04/−2.75 | −1.86 | −1.69 | **0.09** | **0.09** | **0.09** | **0.09** | −1.13 | −2.61/−2.74 |
| NE | −3.08 | −1.95 | −1.17 | 0.92 | **0.21** | 0.93 | 0.33 | −0.40 | −3.61 |

tion stencils exhibit some crossing over near the vertices, this creates no problems in practice.

## 4. Advection results

Similarly to M96, a number of test problems is performed, each with an initial pattern centered in the middle of a panel at 0°, 0°. First is Ritchie's (1987) Gaussian hill of scale diameter 2500 km advected over the North Pole with a solid-body axis of rotation passing though 45°N, 0°E. There are also four cosine bell test cases of Williamson et al. (1992), including advection directly northward (N) over the pole, eastward (E), and northward and eastward each offset by 0.05 rad ($N^+$ and $E^-$, respectively). An extra cosine bell test is performed where the initial direction of advection is northeastward (NE) so that the bell passes directly over four vertices. Each test is performed for one full solid-body rotation.

Figure 3 shows the NE-advected cosine bell for semi-Lagrangian advection on the standard RPM conformal-cubic grid and on the T42 Gaussian grid for 256 steps per rotation (average Courant number of about 0.6). Time traces of the normalized errors for $l_1$, $l_2$, $l_\infty$, mean, variance, minimum, and maximum (as defined by Williamson et al. 1992) are shown in Fig. 4. Note that the error traces show no disruption as the cosine bell passes over the vertices, quite unlike the situation for advection over the poles of a Gaussian latitude–longitude grid (e.g., Figs. 5 and 9 of M96; Jakob et al. 1993). Figure 5 shows the normalized errors for the same test but with a larger average Courant number of about 3.7 (40 steps per rotation). As is usual for semi-Lagrangian advection schemes in tests having steady velocity fields, the errors are much smaller for the larger time steps. The superiority of the conformal-cubic simulation is evident in nearly all respects. A possibly adverse feature of the conformal-cubic simulation is that the variance increases; however, the magnitude of the variance errors remains significantly smaller than for the Gaussian grid. Errors of the means are all very small, although the mean of the conformal-cubic simulation does exceed that of the Gaussian grid.

The eastward-advected cosine bell is shown in Fig. 6 after one rotation of 256 time steps, this time comparing the stretched $\alpha = 0.875$ grid with the Gaussian grid. Normalized errors are shown in Fig. 7, and those for the larger Courant number are displayed in Fig. 8. Again the conformal-cubic simulation is clearly superior to that of the T42 Gaussian grid, although the superiority is not as marked as for NE advection. Results for the northward-advected cosine bell on the T42 Gaussian grid may be found in Figs. 8 and 9 of M96.

To summarize the results concisely, the normalized error measures are shown in Tables 1–7 for each of the tests after one full solid-body rotation of 40 time steps. The N and E cases are shown separately in the tables for the Gaussian grid but are equivalent for the cubic configurations. The $l_1$, $l_2$, and $l_\infty$ errors are given separately, although they produce very similar rankings for the different schemes. The Gaussian hill is more compact than the cosine bell and has correspondingly larger errors for each of the schemes. The cubic grids generally have smaller errors for NE advection (over the vertices) effectively utilizing the increased resolution, but without displaying any singular behavior.

The staggered and unstaggered results are extremely similar to one another. The only real differences occur for the minima (where the staggered results are slightly better) and the maxima (where the unstaggered results are better). In respect of the $l_1$, $l_2$, $l_\infty$, variance, and maxima errors, the RPM conformal-cubic grids perform generally better than the nonorthogonal M96 grids, which in turn outperform the Gaussian grid. Errors in the normalized means are generally small, being

TABLE 6. As in Table 1 but for the error of the minimum (percent of the peak value).

| | Gaussian grid | M96 $\alpha = 1$ | M96 $\alpha = 0.75$ | RPM $\alpha = 1$ | RPM $\alpha = 0.875$ | RPM-B $\alpha = 1$ | RPM-B $\alpha = 0.875$ | RPM-30 $\alpha = 1$ | Reduced Gaussian |
|---|---|---|---|---|---|---|---|---|---|
| Gaussian hill | −0.91 | −0.68 | **−0.46** | −0.90 | −0.78 | −0.89 | −0.76 | −1.28 | −1.07 |
| N/E | −1.35/−1.42 | −1.14 | −1.07 | −1.18 | −1.04 | −1.18 | **−0.96** | −1.36 | −1.18/−1.42 |
| $N^+/E^-$ | −1.27/−1.43 | −1.15 | −1.07 | −1.33 | −1.16 | −1.25 | **−1.03** | −1.39 | −1.20/−1.43 |
| NE | −0.97 | −0.73 | **−0.71** | −1.05 | −0.99 | −0.97 | −1.05 | −1.05 | −1.00 |

TABLE 7. As in Table 1 but for the error of the maximum (percent of the peak value).

| | Gaussian grid | M96 $\alpha = 1$ | M96 $\alpha = 0.75$ | RPM $\alpha = 1$ | RPM $\alpha = 0.875$ | RPM-B $\alpha = 1$ | RPM-B $\alpha = 0.875$ | RPM-30 $\alpha = 1$ | Reduced Gaussian |
|---|---|---|---|---|---|---|---|---|---|
| Gaussian hill | −18.5 | −13.8 | −13.2 | −10.7 | **−9.8** | −14.7 | −12.0 | −21.6 | −21.0 |
| N/E | −1.99/−1.26 | −0.90 | −0.87 | −0.83 | **−0.70** | −0.95 | −0.76 | −0.61 | −0.10/−1.26 |
| $N^+/E^-$ | −1.57/−1.90 | −1.36 | −1.04 | **0.00** | 0.05 | −0.02 | 0.07 | −0.92 | −2.12/−1.90 |
| NE | −2.12 | −1.18 | −0.68 | 0.73 | **0.17** | 0.78 | 0.26 | −0.11 | −2.55 |

smallest for the Gaussian and M96 grids. The minima are generally best for the M96 grids followed by the RPM grids. For each test and each error measure, the stretched grids usually perform better than the unstretched grids. The Gaussian grid performs worse than all the cubic grids for all tests and all error measures except the mean.

In recent years a number of global spectral models have adopted reduced Gaussian grids (Hortal and Simmons 1991; Courtier and Naughton 1994) in which the number of grid points on latitude circles is progressively reduced nearer the poles. The final two columns of the tables compare semi-Lagrangian advection tests on the RPM grid with $N = 30$ (having 5402 points) with similar tests on a reduced T42 Gaussian grid having 5448 points. The number of points on the latitude rows of the reduced Gaussian grid are 12, 16, 20, 24, 30, 36, 45, 50, . . . , 128 proceeding from the pole to the equator. Semi-Lagrangian advection was performed by the method of McGregor (1993); where interpolated values were required from adjacent rows, cubic interpolation along those rows was used.

As is to be expected, easterly advection along the equator produces virtually identical errors for the reduced and full Gaussian grids; for the other advection tests, the reduced grid shows some loss of accuracy with the present implementation. The $N = 30$ RPM grid produces fairly similar errors to the reduced Gaussian grid for Ritchie's test; for the other tests the RPM grid turns out to be generally more accurate.

## 5. Concluding comments

A semi-Lagrangian advection scheme has been proposed for the conformal-cubic grid of Rančić et al. (1996) and successfully applied to six test problems of solid-body rotation. The grid has quasi-uniform resolution, although it is not as uniform as the nonorthogonal cubic grids studied by M96; stretched versions are slightly more uniform. In advection tests the conformal grid performed most accurately overall, being superior to the M96 scheme, and better still than tests on the Gaussian latitude–longitude grid. Tests with a coarser conformal-cubic grid produced similar or better accuracy than semi-Lagrangian tests on a reduced Gaussian grid having a similar number of grid points.

The conformal scheme is slightly more expensive than the nonorthogonal M96 scheme; instead of an analytic formula, it requires two iterations to determine the departure points in terms of panel indices. However, the conformal scheme has the advantage of always being able to use a centered interpolation stencil. It is also well suited to quasi-cubic interpolation. The semi-Lagrangian advection schemes on the cubic grids are efficient and run only 10%–20% slower than on a Gaussian grid having a similar number of points. The reduced Gaussian grid requires extra interpolations and runs at a quite similar speed to the cubic grids.

Although the vertices of the grid represent singularities (meeting at 120° instead of being orthogonal), they are easily handled in the finite-difference scheme. There is no disruption as patterns are advected over the vertices, quite unlike the situation for advection over the poles of a Gaussian grid.

Advection tests were also carried out on a B-staggered version of the grid and found to perform as well as the unstaggered tests. It was demonstrated that the unstaggered departure points may be accurately and cheaply interpolated to provide staggered-grid departure points. In the near future it is planned to produce a shallow-water model on a B-staggered conformal-cubic grid.

*Acknowledgments.* The author is most grateful to Miodrag Rančić, Jim Purser, and Fedor Mesinger for generously providing their algorithms that calculate the grid information for the conformal-cubic grid. Martin Dix, Hal Gordon, Jim Purser, and two anonymous reviewers provided valuable comments on the manuscript.

APPENDIX A

### Gnomonic Transformations

*a. 3D (X, Y, Z) on the sphere to 3D (A, B, C) on the cube*

$$(A, B, C) = \frac{(X, Y, Z)R}{\max(|X|, |Y|, |Z|)}; \qquad \text{(A1)}$$

*b. 3D (A, B, C) on the cube to 2D (a, b, p) on the cube.*

This transformation may be performed by branching computations; the following alternative equations avoid branching computations. The panel index, $p$, is given by

$$p = \max[A_{\text{int}}(3A_{\text{int}} - 3), B_{\text{int}}(7B_{\text{int}} - 3), C_{\text{int}}(5C_{\text{int}} - 3)]/2, \quad \text{(A2)}$$

where

$$A_{\text{int}} = \text{int}\left(\frac{A}{R}\right), \; B_{\text{int}} = \text{int}\left(\frac{B}{R}\right), \; C_{\text{int}} = \text{int}\left(\frac{C}{R}\right) \quad \text{(A3)}$$

and "int" indicates the truncated integer value. The Cartesian coordinate position $(a, b, p)$ on a panel of the cube is then

$$a = E_{p1}A + E_{p2}B + E_{p3}C \quad \text{(A4)}$$

$$b = F_{p1}A + F_{p2}B + F_{p3}C, \quad \text{(A5)}$$

where the nonzero members of matrices **E** and **F** are

$$E_{02} = E_{12} = -E_{23} = -E_{33} = E_{41} = E_{51} = F_{03} = -\mathrm{F}_{11} = -F_{21} = -F_{32} = -F_{42} = F_{53} = 1.$$

*c. 2D (a, b, p) on the cube to 3D (A, B, C) on the cube*

$$A = R, \quad B = a, \quad C = b \quad \text{for} \quad p = 0, \quad \text{(A6)}$$

$$A = -b, \quad B = a, \quad C = R \quad \text{for} \quad p = 1, \quad \text{(A7)}$$

$$A = -b, \quad B = R, \quad C = -a \quad \text{for} \quad p = 2, \quad \text{(A8)}$$

$$A = -R, \quad B = -b, \quad C = -a \quad \text{for} \quad p = 3, \quad \text{(A9)}$$

$$A = a, \quad B = -b, \quad C = -R \quad \text{for} \quad p = 4, \quad \text{(A10)}$$

$$A = a, \quad B = -R, \quad C = b \quad \text{for} \quad p = 5; \quad \text{(A11)}$$

*d. 3D (A, B, C) on the cube to 3D (X, Y, Z) on the sphere*

$$(X, Y, Z) = \frac{(A, B, C)}{(A^2 + B^2 + C^2)^{1/2}} R. \quad \text{(A12)}$$

APPENDIX B

## Specification of Tangent Vectors on Different Panels

Given a unit tangential vector along an $x$ axis at $(x, y, 0)$,

$$\hat{\mathbf{x}}_0 = (\gamma_1, \gamma_2, \gamma_3) \quad \text{(B1)}$$

expressed in Cartesian coordinates, it can be seen by the symmetries of (A6)–(A11) that the corresponding tangential vectors $\hat{\mathbf{x}}_n$ at $(x, y, n)$ on the other panels are given by

$$\hat{\mathbf{x}}_1 = (-\gamma_3, \gamma_2, \gamma_1) \quad \text{(B2)}$$

$$\hat{\mathbf{x}}_2 = (-\gamma_3, \gamma_1, -\gamma_2) \quad \text{(B3)}$$

$$\hat{\mathbf{x}}_3 = (-\gamma_1, -\gamma_3, -\gamma_2) \quad \text{(B4)}$$

$$\hat{\mathbf{x}}_4 = (\gamma_2, -\gamma_3, -\gamma_1) \quad \text{(B5)}$$

$$\hat{\mathbf{x}}_5 = (\gamma_2, -\gamma_1, \gamma_3). \quad \text{(B6)}$$

Corresponding tangential vectors $\hat{\mathbf{y}}_n$ along the $y$ axes are given by

$$\hat{\mathbf{y}}_n = \mathbf{r} \times \hat{\mathbf{x}}_n, \quad \text{(B7)}$$

where $\mathbf{r}$ is the position vector with origin at the center of the sphere.

APPENDIX C

## Inverse Index Determination on a Panel

The description here is given in terms of the quadruple-resolution grid. Given the projected values $(a, b)$ on a known panel of the cube, we wish to find the position on the panel in terms of index values $(I, J)$, where $I$ and $J$ need not be integers but satisfy $1 \leq I < 4N + 1$ and $1 \leq J < 4N + 1$. Note that when $I$ and $J$ both have integer values, the corresponding $(a, b)$ coincides with a grid point.

An iterative grid point near $(I, J)$ is denoted by $(i, j)$; the area surrounding it is divided into four quadrants. In "northeast" quadrants (valid for the triangular region $0 \leq I - i \leq 1$, $0 \leq J - j < I - i$) simple bilinear interpolation gives for the $a$-component

$$a = a_{ij} + (I - i)(a_{i+1,j} - a_{ij}) + (J - j)(a_{ij+1} - a_{ij}). \quad \text{(C1)}$$

This formula can be generalized to cover all four quadrants

$$a = a_{ij} + i'(I - i)(a_{i+i',j} - a_{ij}) + j'(J - j)(a_{ij+j'} - a_{ij}), \quad \text{(C2)}$$

where the desired quadrant is selected as described below by allocating particular values to the sign functions $i' = \pm 1$, $j' = \pm 1$. The corresponding expression for the $b$-component is

$$b = b_{ij} + i'(I - i)(b_{i+i',j} - b_{ij}) + j'(J - j)(b_{ij+j'} - b_{ij}). \quad \text{(C3)}$$

The iterative solution proceeds in the following manner. A first guess is denoted by $(I_0, J_0) = (1 + 2N + 2Na/R, 1 + 2N + 2Nb/R)$. The quadrant is selected from the previous guess $(I_0, J_0)$ with

$$i' = \text{sign}(1, I_0 - i), \quad j' = \text{sign}(1, J_0 - j), \quad \text{(C4)}$$

where

$$i = \text{nint}(I_0), \quad j = \text{nint}(J_0), \quad \text{(C5)}$$

and where "sign" and "nint" refer to the standard Fortran functions. Writing

$$\delta_a a = a_{i+i',j} - a_{ij}; \quad \delta_b a = a_{ij+j'} - a_{ij} \quad \text{(C6)}$$

$$\delta_a b = b_{i+i',j} - b_{ij}; \quad \delta_b b = b_{ij+j'} - b_{ij}, \quad \text{(C7)}$$

the next iteration gives the following noninteger $I$ and $J$ values

$$I = i + \frac{(a - a_{i,j})\delta_b b - (b - b_{i,j})\delta_b a}{i'(\delta_a a \delta_b b - \delta_b a \delta_a b)} \quad \text{(C8)}$$

and

$$J = j + \frac{(b - b_{i,j})\delta_a a - (a - a_{i,j})\delta_a b}{j'(\delta_a a \delta_b b - \delta_b a \delta_a b)}. \quad \text{(C9)}$$

Equations (C4)–(C9) are repeated until convergence is achieved (two iterations in practice).

The above equations refer to the quadruple-resolution grid. These $I$ and $J$ are simply converted to regular grid values

$$I_{\text{regular}} = \frac{I + 3}{4}, \; J_{\text{regular}} = \frac{J + 3}{4}. \quad \text{(C10)}$$

Exactly the same procedure can be applied for staggered B-grid calculations using the identical quadruple-resolution grid, but in this case the $I$ and $J$ convert to

$$I_{\text{B-grid}} = \frac{I + 1}{4}, \; J_{\text{B-grid}} = \frac{J + 1}{4}, \quad \text{(C11)}$$

where the staggered B-grid indexing on any panel is defined such that $1/2 \leq I_{\text{B-grid}} < N + 1/2$ and $1/2 \leq J_{\text{B-grid}} < N + 1/2$.

## REFERENCES


Courtier, P., and M. Naughton, 1994: A pole problem in the reduced Gaussian grid. *Quart. J. Roy. Meteor. Soc.*, **120,** 1389–1407.

Hortal, M., and A. J. Simmons, 1991: Use of reduced grids in spectral models. *Mon. Wea. Rev.*, **119,** 1057–1074.

Jakob, R., J. J. Hack, and D. L. Williamson, 1993: Solutions to the shallow water test set using the spectral transform method. Tech. Note NCAR/TN-388+STR, National Center for Atmospheric Research, Boulder, Colorado, 79 pp.

Marchuk, G. I., 1974: *Numerical Methods in Weather Prediction.* Academic Press, 277 pp.

McGregor, J. L., 1993: Economical determination of departure points for semi-Lagrangian models. *Mon. Wea. Rev.*, **121,** 221–230.

——, 1996: Semi-Lagrangian advection on a cubic gnomonic projection of the sphere. *Atmos.–Ocean,* in press.

——, and L. M. Leslie, 1977: On the selection of grids for semi-implicit schemes. *Mon. Wea. Rev.*, **105,** 236–238.

——, K. J. Walsh, and J. J. Katzfey, 1993: Nested modelling for regional climate studies. *Modelling Change in Environmental Systems,* A. J. Jakeman, M. B. Beck and M. J. McAleer, Eds., John Wiley, 367–386.

Mesinger, F., and A. Arakawa, 1976: *Numerical Methods Used in Atmospheric Models.* GARP Publications Series 17, Vol. 1, WMO, 66 pp.

Rančić, M., R. J. Purser, and F. Mesinger, 1996: A global shallow water model using an expanded spherical cube: Gnomonic versus conformal coordinate. *Quart. J. Roy. Meteor. Soc.,* in press.

Ritchie, H., 1987: Semi-Lagrangian advection on a Gaussian grid. *Mon. Wea. Rev.*, **115,** 608–619.

——, C. Temperton, A. Simmons, M. Hortal, T. Davies, D. Dent, and M. Hamrud, 1995: Implementation of the semi-Lagrangian method in a high-resolution version of the ECMWF forecast model. *Mon. Wea. Rev.*, **123,** 489–514.

Rivest, C., A. Staniforth, and A. Robert, 1994: Spurious resonant response of semi-Lagrangian discretizations to orographic forcing: Diagnosis and solution. *Mon. Wea. Rev.*, **122,** 366–376.

Sadourny, R., 1972: Conservative finite-difference approximations of the primitive equations on quasi-uniform spherical grids. *Mon. Wea. Rev.*, **100,** 136–144.

Williamson, D. L., J. B. Drake, J. J. Hack, R. Jakob, and P. N. Swartztrauber, 1992: A standard test set for numerical approximations to the shallow water equations in spherical geometry. *J. Comput. Phys.*, **102,** 211–224.